

Quadrupolar resonance spectroscopy of individual nuclei using a room-temperature quantum sensor

S. Alex Breitweiser,^{†,‡,¶,⊥} Mathieu Ouellet,^{†,‡} Tzu-Yung Huang,^{‡,#} Tim H. Taminiau,^{§,||} and Lee C. Bassett^{*,‡}

†These two authors contributed equally

‡Quantum Engineering Laboratory, Department of Electrical and Systems Engineering, University of Pennsylvania, 200 S. 33rd St. Philadelphia, Pennsylvania, 19104, USA

¶Department of Physics and Astronomy, University of Pennsylvania, 209 S. 33rd St. Philadelphia, Pennsylvania 19104, USA

§ QuTech, Delft University of Technology, PO Box 5046, 2600, GA Delft, The Netherlands

|| Kavli Institute of Nanoscience Delft, Delft University of Technology, PO Box 5046, 2600, GA Delft, The Netherlands

⊥Present address: IBM Research, 1101 Kitchawan Rd Yorktown Heights, NY 10598, USA

#Present address: Nokia Bell Labs, 600 Mountain Avenue, Murray Hill, NJ 07974, USA

E-mail: lbassett@seas.upenn.edu

Abstract

Nuclear quadrupolar resonance (NQR) spectroscopy reveals chemical bonding patterns in materials and molecules through the unique coupling between nuclear spins and local fields. However, traditional NQR techniques require macroscopic ensembles of nuclei to yield a detectable signal, which obscures molecule-to-molecule variations. Solid-state spin qubits, such as the nitrogen-vacancy (NV) center in diamond, facilitate the detection and control of individual nuclei through their local magnetic couplings.

Here, we use NV centers to perform NQR spectroscopy on their associated nitrogen-14 (^{14}N) nuclei at room temperature. In mapping the nuclear quadrupolar Hamiltonian, we resolve minute variations between individual nuclei. The measurements reveal correlations between the Hamiltonian parameters associated with the NV center’s electronic and nuclear spin states, as well as a previously unreported symmetry-breaking quadrupolar term. We further design pulse sequences to initialize, readout, and control the quantum evolution of the ^{14}N nuclear state using the nuclear quadrupolar Hamiltonian.

Keywords

Nuclear quadrupolar resonance, Spectroscopy, NV centers

Nuclear Quadrupole Resonance (NQR) spectroscopy detects interactions between nuclear electric quadrupole moments and local electric field gradients, aiding the study of molecular structures at low bias magnetic field.¹⁻³ NQR spectroscopy is widely applied in security for explosive and drug detection,⁴⁻⁶ pharmaceutical analysis of powders,⁷⁻⁹ and thermometry.^{10,11} Due to the unique fields experienced by nuclei at each site, set primarily by the valence electrons and, therefore, the corresponding chemical bonds, NQR studies reveal a wealth of information that can be used to identify and characterize molecules and bulk materials. However, due to the small magnetic signal generated by each nucleus, traditional radio-frequency NQR is limited to use with macroscopic samples that contain large nuclear ensembles. The ability to perform NQR on individual nuclear sites would open up the possibility of studying molecule-to-molecule variations and dynamical changes due to local fields and structural changes, *e.g.*, protein folding and drug-target interactions.

Quantum sensors based on optically active defects in semiconductors allow for investigations of much smaller nuclear ensembles. Defect-based quantum sensors such as the diamond

nitrogen-vacancy (NV) center host electronic spin states that can be initialized and measured with laser light and manipulated with microwave signals at room temperature. The electron spin qubits interact with proximal nuclear spins through unique magnetic hyperfine couplings that are determined by their positions.¹² Using Dynamical Decoupling (DD) control sequences, it is possible to resonantly amplify these hyperfine couplings,¹³ allowing high precision characterization and control of individual nuclei.¹⁴⁻¹⁹ NV-center quantum sensors have been employed along with DD sequences to perform NQR spectroscopy of small nuclear ensembles in deuterated molecules²⁰ and in hexagonal boron nitride crystals.^{21,22} In other regimes, NV-center ensembles have been used to boost the sensitivity of traditional NQR detectors for macroscopic powder samples.³ However, accessing individual nuclei and retrieving their quadrupolar Hamiltonian has remained an open challenge.

In this work, we demonstrate DD-based, room-temperature NQR spectroscopy of the nitrogen-14 (^{14}N) nuclei intrinsic to individual NV centers. In this way, the NV centers serve as both quantum sensors and as analogs of individual molecules. The measurements reveal considerable variations in the ^{14}N quadrupolar and hyperfine parameters among different NV centers, as well as a previously unreported term in the nuclear quadrupolar Hamiltonian that results from symmetry breaking. We further observe correlations between the nuclear Hamiltonian parameters and the electronic Zero-Field Splitting (ZFS) parameters, highlighting the potential of NQR spectroscopy to reveal details of local chemical structure and deformations due to electric or strain fields. Finally, we design and implement DD sequences that utilize the ^{14}N quadrupolar Hamiltonian to facilitate initialization and arbitrary quantum control of the ^{14}N nuclear spin.

Electron-nuclear interactions in diamond NV centers

The NV center (Figure 1a) consists of one substitutional ^{14}N coupled to a vacancy in the diamond lattice. In its negatively charged state, the NV center hosts an electronic spin-1

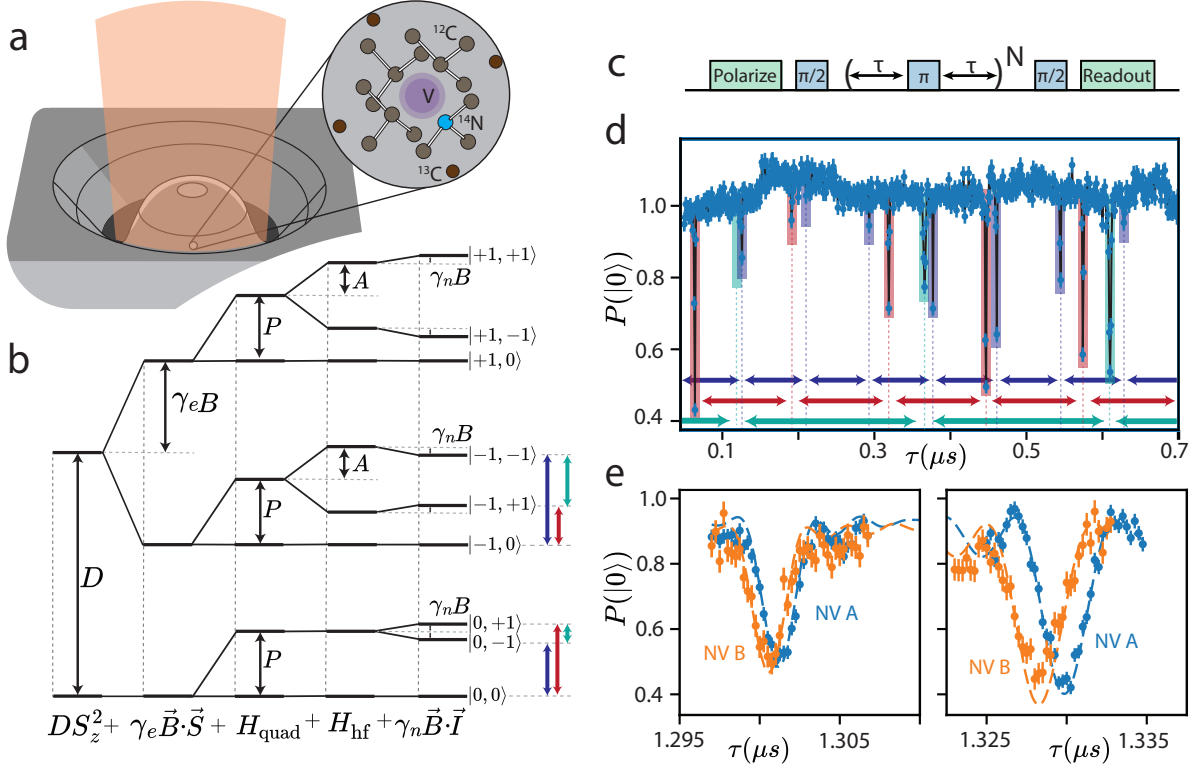


Figure 1: **Electron-nuclear interactions in ^{14}NV centers** (a) Model of a diamond NV center located within a solid immersion lens, composed of an electronic spin (purple) coupled to a ^{14}N nucleus (blue). (b) Pictorial representation of the Hamiltonian terms for ^{14}NV . (c) Schematic of a DD spectroscopy sequence. Initial and final $\frac{\pi}{2}$ pulses are in opposite directions, while decoupling π pulses are XY8 symmetrized. (d) DD NQR features corresponding to the $|m_I = \pm 1\rangle$ to $|m_I = 0\rangle$ transitions (dips marked purple and red) appear in the presence of an off-axis magnetic field ($N = 64$, $B = 193$ G). A third series of dips corresponding to the $|m_I = \pm 1\rangle$ transition (marked green) appears due to the quadrupolar asymmetry parameter, even without an off-axis magnetic field. Panel (b) displays the energy levels associated with the peaks. (e) DD spectra for two different NV centers (blue and orange), here with $N = 32$ pulses repetitions, reflect significant differences in the ^{14}N quadrupolar Hamiltonian. Data are shown with markers, along with best-fit simulation results as dashed lines.

state that undergoes a spin-dependent optical pumping transition, allowing the spin state to be initialized and read out optically.²³ This electronic spin interacts with the intrinsic ^{14}N nuclear spin within the NV center ($\approx 99.7\%$ spin-1 ^{14}N in natural abundance), as well as with ^{13}C nuclei in the surrounding diamond lattice (spin- $\frac{1}{2}$, $\approx 1.1\%$ natural abundance) and any other nearby nuclear spins. In the isotropic case, ignoring the effects of strain or electric fields, the general Hamiltonian comprising the electron spin interacting with a single nuclear spin is given by

$$H = DS_z^2 + E(S_X^2 - S_Y^2) + \gamma_e \vec{B} \cdot \vec{S} + H_{\text{quad}} + H_{\text{hf}} + \gamma_n \vec{B} \cdot \vec{I}, \quad (1)$$

where $\vec{S} = (S_X, S_Y, S_Z)$ is the electronic spin operator, $\vec{I} = (I_X, I_Y, I_Z)$ is the nuclear spin operator, γ_e (γ_n) is the electronic (nuclear) gyromagnetic ratio, and $B = (B_X, B_Y, B_Z)$ is the external magnetic field. Figure 1b shows this Hamiltonian diagrammatically for the specific example of the NV-center's intrinsic ^{14}N nucleus. The first two terms represent electronic zero-field splitting (ZFS), followed by the Zeeman term for electronic spins. This is succeeded by the nuclear quadrupolar term and hyperfine coupling and the Zeeman term for nuclear spins. The term H_{hf} represents the hyperfine interaction, which takes the general form

$$H_{\text{hf}} = \vec{S} \cdot \mathbf{A} \cdot \vec{I} \quad (2)$$

where \mathbf{A} is the hyperfine interaction tensor. For ^{14}NV , H_{hf} takes the simplified form:

$$H_{\text{hf}} = A_Z S_Z I_Z + A_{\perp} (S_X I_X + S_Y I_Y), \quad (3)$$

where A_Z and A_{\perp} are the parallel and perpendicular hyperfine coupling strengths. The second term in Eq. 3 generally does not affect the electron-nuclear dynamics due to the large mismatch in energy splitting between the electron and nuclear spin states, leaving the parallel term as the primary hyperfine-coupling effect.

The term H_{quad} represents the nuclear quadrupolar Hamiltonian, which is nonzero for nuclear species with total nuclear spin $I \geq 1$. The quadrupolar Hamiltonian can, in general, be written as²⁴

$$H_{\text{quad}} = \frac{eQV_{ZZ}}{4I(2I-1)} [3I_Z^2 - I(I+1) + \frac{V_{XX} - V_{YY}}{2V_{ZZ}}(I_+^2 + I_-^2)] \quad (4)$$

where e is the electron charge, Q is the quadrupolar moment unique to each nuclear isotope, $V_{ZZ} = \partial^2 V / \partial z^2$ is the electric field gradient along the principal nuclear axis, and V_{XX} and V_{YY} are the electric field gradients in the perpendicular plane. The principal axes are chosen so that $|V_{ZZ}| > |V_{XX}| > |V_{YY}|$, and the electric field gradient is diagonal in this basis. For a particular nucleus, Eq. (4) takes the simplified form

$$H_{\text{quad}} = PI_Z^2 + \alpha(I_+^2 + I_-^2), \quad (5)$$

where P and α are constant parameters representing the quadrupolar splitting and asymmetry parameters, respectively.

Although the nuclear quadrupolar Hamiltonian term is distinct from the electronic spin, its effects on the electronic spin can be observed *via* the hyperfine interaction using DD sequences as shown in Figure 1c. Transverse terms in H_{hf} (the second term in Eq. 3) lead to rotations of the nuclear state that depend on the electron spin projection. DD sequences amplify this interaction since multiple small rotations accumulate when the spacing between pulses is resonant with the hyperfine-shifted frequency of the nuclear Larmor precession, causing resonant series to emerge in DD spectra.¹³

Figure 1d shows an example of a DD NQR spectrum in which three distinct resonance series can be observed. The series correspond to electron-spin-dependent transitions between the ^{14}N nuclear states as indicated in Fig. 1b. As discussed in the next section, the physics responsible for transitions between nuclear states with $|m_I = 0\rangle \leftrightarrow |m_I = \pm 1\rangle$ is different from those transitions between $|m_I = \pm 1\rangle$ states. Nevertheless, the observation of all three

resonance series constitutes a complete measurement of the nuclear quadrupolar Hamiltonian (Eq. 5), together with A_Z . Since the DD sequence extends the coherence lifetime of the electronic spin, this method allows extremely precise determination of P for each nucleus and also reveals the existence of small α Hamiltonian terms that had previously not been detected nor considered.²³

DD NQR spectroscopy

The ^{14}N nucleus intrinsic to the NV center represents a convenient testbed to illustrate the physics of DD-based NQR. Ideally, the C_{3v} symmetry of the NV center should cause the asymmetry quadrupolar parameter α to vanish. Moreover, in the presence of a purely longitudinal magnetic field ($B_X = B_Y = 0$), the axially-symmetric hyperfine Hamiltonian of Eq. 3 does not generate nuclear spin rotations under DD sequences, since the magnetic field direction experienced by the nucleus is independent of the electron spin projection. In real systems with reduced symmetry, however, both of these conditions are relaxed.

In the presence of a weak transverse magnetic field ($B_X \ll B_Z$) an effective perpendicular hyperfine coupling term appears due to spin mixing,²⁵ leading to an approximate hyperfine Hamiltonian given by

$$H_{\text{hf}} \approx A_Z S_Z I_Z + F \frac{\gamma_N B_X A_{\perp}}{\gamma_e B_Z} S_Z I_X, \quad (6)$$

where F is a constant that is particular to the ^{14}N nuclear isotope.²⁶ Previous authors have used this effective hyperfine interaction to observe nuclear quadrupolar interactions for NV ensembles using electron spin-echo envelope modulation,²⁷ to perform dc vector magnetometry using single NV centers²⁶ and to realize high fidelity gates.²⁸ We use it in order to quantify the quadrupolar Hamiltonian parameters *via* DD NQR spectroscopy. In a DD control sequence with appropriate pulse spacing, the $S_Z I_X$ term in the effective hyperfine Hamiltonian facilitates electron-spin-dependent rotations of the ^{14}N spin (see Figure 1c), in analogy with the case for ^{13}C nuclei.¹³ The rotations manifest in DD spectra as two distinct

resonance series, each corresponding to one of the $|m_I\rangle = 0$ to $|m_I = \pm 1\rangle$ transitions, with spacing given by

$$\tau_k \approx \frac{(2k+1)\pi}{2P \pm A_z \mp \omega_N} \quad (7)$$

where $\omega_N = \gamma_N B$.

Figure 1e shows the DD NQR spectra obtained by sweeping the pulse spacing near two such transition resonances for two different NV centers. The shift in resonance position reflects differences in P and A_Z for these two NV centers. We use numerical simulations to fit DD NQR spectra acquired using different N around these two resonances; see the Supporting Information, Sec. II. Table 1 shows NQR spectroscopy results for six NV centers located within the same diamond sample (see the Supporting Information, Fig. S3, for the underlying data). Interestingly, the values of P and A_Z show a variance one order of magnitude larger than the measurement uncertainty. In particular, NV A exhibits values for P and A_Z that differ by several kHz from the other NVs in this sample. NV A is also the only NV under a diamond solid immersion lens (SIL). These milled structures are used to minimize optical losses caused by total internal reflection and spherical aberration (See Figure 1a).^{29,30} Yet, they are recognized to influence the local strain field at the NV centers,³¹ consequently affecting the NV Hamiltonian.^{32,33}

Table 1: Electronic ZFS, hyperfine, and ^{14}N quadrupolar parameters for each NV studied.

NV	D (MHz)	E (MHz)	A_Z (kHz)	P (kHz)	β
A	2859.20(2)	8.33(4)	2168.1(1)	4934.9(1)	0.0016(2)
B	2870.47(2)	7.51(4)	2164.7(1)	4939.5(1)	0.0039(3)
C	2870.39(2)	7.63(4)	2163.5(5)	4939.4(2)	0.0095(4)
D	2870.37(1)	7.58(3)	2165.0(3)	4939.2(1)	0.0175(6)
E	2872.20(3)	7.58(4)	2162.9(4)	4936.9(2)	0.0205(4)
F	2870.41(2)	7.04(3)	2162.9(4)	4940.7(2)	0.0082(4)

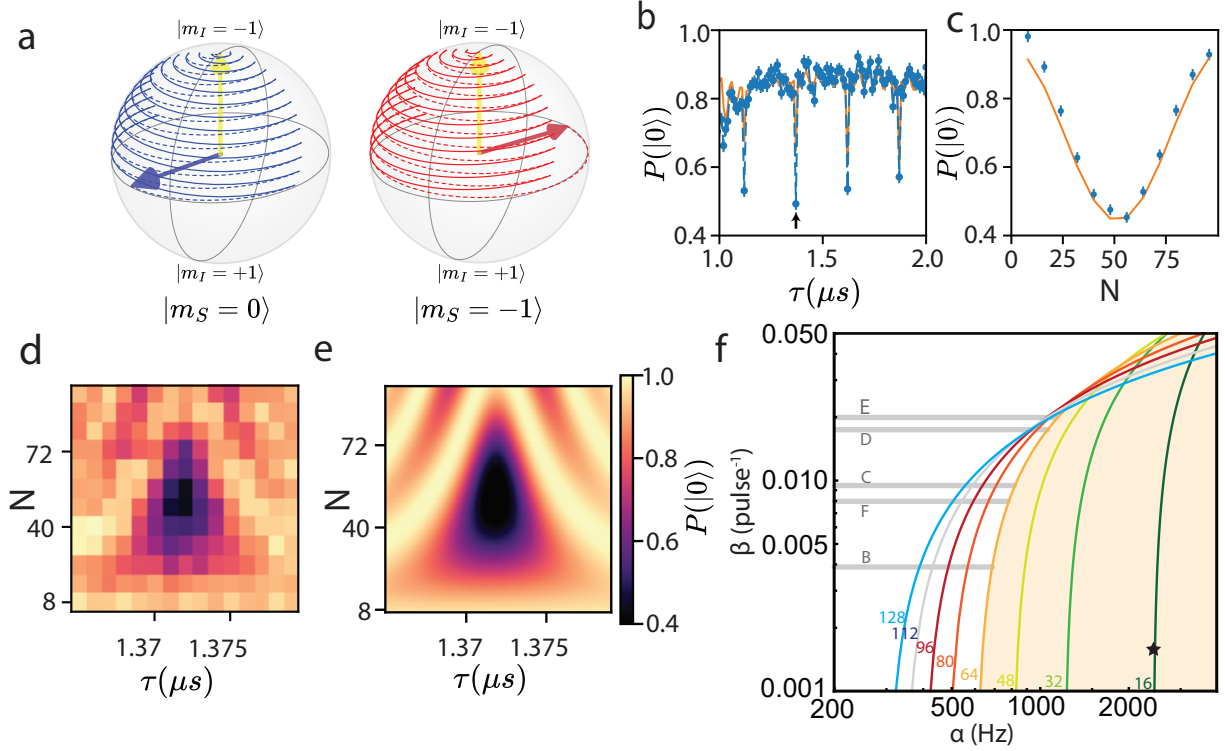


Figure 2: **Forbidden transitions** (a) Evolution of the nuclear spin in the $|m_I = \pm 1\rangle$ manifold when the electronic spin is in the state $|m_s = 0\rangle$ (blue) and $|m_s = -1\rangle$ (red) for a tuned DD sequence with $N = 12$. (b) DD spectroscopy data for NV A (blue points with dashed line) and simulation (solid orange curve) for $N = 32$. (c) The measured electron spin projection (blue markers) as a function of N for fixed $\tau = 1.372 \mu\text{s}$ (black marker in (b)) agrees with simulations (solid orange curve). (d) DD spectroscopy data as a function of τ and N , which is fit using simulations (e) to determine the value of α . Error bars in (d) are comparable to those in (b) and (c). (f) Detection limit for α as a function of β for tuned DD sequences with different N ; the detection limit is the situation where the signal-to-noise ratio exceeds 1. The noise floor is assumed to be constant at $P(|0\rangle) = 0.2$. The shaded area represents the detection threshold for the sequence applied experimentally. The star marks the value for NV A.

Forbidden quadrupolar transitions

Although the α_i term in the ^{14}N quadrupolar Hamiltonian vanishes for the ideal case of C_{3v} symmetry, local perturbations such as strain and electric fields can distort the electronic wavefunctions, leading to nonzero transverse electric-field gradients at the ^{14}N position. When α is nonzero, the second term in Eq. (5) directly couples the $|m_I = -1\rangle$ and $|m_I = +1\rangle$ nuclear states, causing nuclear transitions to occur that are typically symmetry forbidden. Figure 2a illustrates these dynamics for a suitably tuned DD sequence, whereby the nuclear spin evolves in the $|m_I = +1\rangle$ manifold according to slightly different rotation axes depending on the electronic spin state; after many pulses, the nuclear spin evolves into orthogonal spin states. The resulting entanglement between electronic and nuclear spins manifests as a reduced signal amplitude for these carefully tuned pulse sequences. DD spectroscopy of NV A (Fig. 2b) reveals the presence of these forbidden transitions as a series of sharp, periodic resonances with a spacing given by

$$\tau_k \approx \frac{(2k + 1)\pi}{2(A_Z - 2\omega_N)}, \quad (8)$$

where $\omega_N = \gamma_N B$. Section VII in the Supporting Information includes a derivation of this expression.

In analogy to the typical phenomena of DD resonances (as in Fig. 1c), whereby A_{\perp} induces S_z -dependent rotations between states with $\Delta m_I = 1$, here the nonzero α term induces S_z -dependent transitions between $|m_I = \pm 1\rangle$ states. When α is small, many pulses are needed in order to accumulate a measurable rotation angle. Figure 2c shows the evolution of the DD signal as a function of N ; the contrast is reduced by approximately $\frac{1}{3}$ due to the thermal occupation probability of the uncoupled $|m_I = 0\rangle$ state. By varying both τ and N (Fig. 2f) around a particular resonance, we map out the full dynamics of these forbidden quadrupolar resonances. A fit using numerical simulations (Fig. 2f) yields a best-fit value of $\alpha = 2\pi \times 2.429(12)$ kHz. The ratio $\alpha/P = 5 \times 10^{-4}$ illustrates how a tiny Hamiltonian

parameter can have a substantial impact on nuclear dynamics and be measured with high precision using DD spectroscopy.

The sensitivity of the DD-based measurement is limited by intrinsic decoherence mechanisms (captured by T_2) and by pulse errors.³⁴ For the sequences we consider, the total experimental sequence times are much shorter than the intrinsic decoherence time (typically $T_2 \approx 1\text{ms}$ at room temperature), and the contrast decay is dominated by pulse errors, which we model using an exponential envelope, $e^{-\beta N}$. This envelope constrains the practical detection limit of α , shown in Figure 2b as a set of curves for different N as a function of β .

Of the six NV centers we studied, we only observed forbidden transitions for NV A. We propose two reasons for this observation. First, NV A may experience larger-than-average symmetry breaking from transverse strain or electric fields due to its location at the center of a milled SIL, and hence a larger value of α . This is supported by measurements of the electronic ZFS D and E (Table 1) are significantly different than for other NV centers in the sample. Moreover, NV A features the smallest β of the sample and, subsequently, the lowest detection limit. Figure 2f shows the β values for the other NV centers along with a shaded region corresponding to the $N < 64$ limit we experimentally investigated; we expect that α for these NV centers is outside the detection region.

Nuclear initialization and coherent evolution

In addition to their use in sensing, DD sequences can be used to achieve precise control over individual spin states.¹³⁻¹⁵ Combinations of conditional and non-conditional gates can be used to construct protocols for nuclear-spin initialization, unitary control, and entanglement with the electron spin.¹⁴ Figure 3a shows a sequence used to probe ^{14}N spin initialization. Here, two DD sequences functioning as CNOT gates transfer the population from the electron to the nuclear spin states, and a subsequent electron-spin free-precession sequence probes the

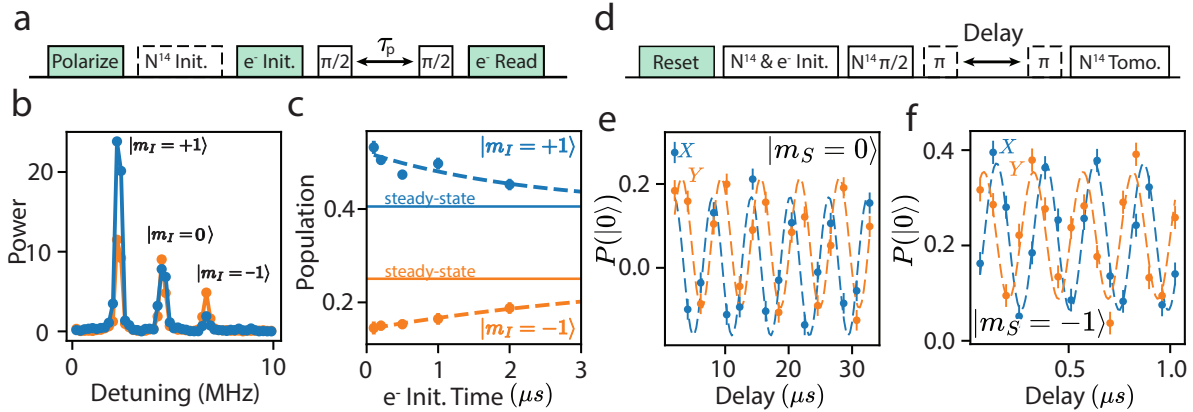


Figure 3: **Initialization and Coherent Evolution** (a) Experimental sequence used to probe initialization of the ^{14}N nuclear spin. (b) Power spectra of the free-precession data acquired without (orange) and with (blue) a DD-based initialization sequence. (c) $|m_I = +1\rangle$ (blue markers) and $|m_I = -1\rangle$ (orange markers) populations fitted from Ramsey data while varying the amount of green time used to reinitialize the electron state. Exponential fits (dotted lines) show the population difference decaying to the steady state values (solid horizontal lines). (d) Pulse sequence used to measure the free induction decay of the ^{14}N nuclear spin. (e,f) Oscillations of the X (blue markers) and Y (orange markers) projection of the ^{14}N nuclear spin within the $|m_I = +1\rangle / |m_I = -1\rangle$ manifold during free evolution while the electron spin is in the (e) $|m_S = 0\rangle$ and (f) $|m_S = -1\rangle$ state.

resulting nuclear population. The electron precession exhibits three oscillation frequencies associated with the ^{14}N spin states, resolved by the A_Z hyperfine coupling (Fig. 3b). The relative amplitudes of these three oscillations, extracted from the power spectrum (Fig. 3b) reflect the nuclear spin occupation probabilities. In this case, the DD initialization sequence applied to a forbidden transition of NV A transfers population from the $|m_I = -1\rangle$ state directly to $|m_I = +1\rangle$, further confirming the physical interpretation of these resonances.

The data in Fig 3b show that the ^{14}N nuclear spin is partially polarized even without the ^{14}N initialization sequence. This is due to the off-axis hyperfine interaction in the optically excited state.³⁵ By sweeping the duration of green illumination used to reset the electron spin, the non-equilibrium nuclear population lasts for several microseconds (Figure 3c) before returning to the steady state values, consistent with other studies on the ^{14}N nuclear spin population.³⁶ Nuclear tomography on the ^{14}N using the electronic spin confirms the effectiveness of the initialization sequence (Figure 3d). Oscillations in the ^{14}N nuclear

spin projection within the $|m_I = +1\rangle / |m_I = -1\rangle$ manifold during free evolution, observable while the electron spin is in the $|m_S = 0\rangle$ and $|m_S = -1\rangle$ states, are evident in Figures 3e and 3f. Section V of the Supporting Information includes further information about the initialization and tomography sequences.

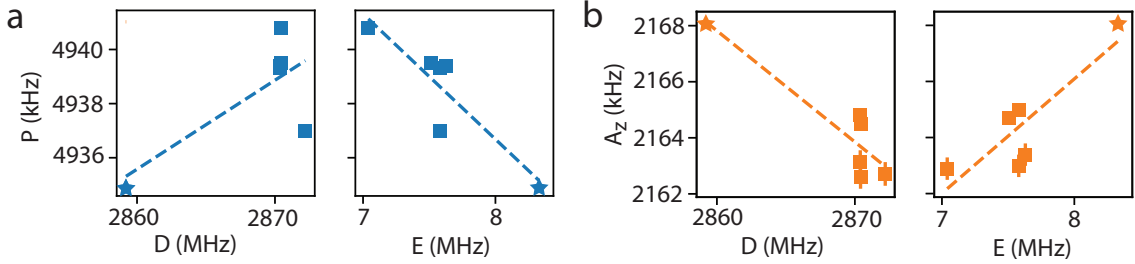


Figure 4: **Impact of ZFS parameters** (a) Measured P parameters for ^{14}N , derived from DD spectroscopy, plotted against the electron ZFS parameters D and E electron splitting parameters derived from zero-field ESR data. (b) Measured A_z parameters for ^{14}N , similarly plotted against D and E . Dashed lines indicate linear fits. Error bars are comparable in size to the markers. NV A is indicated in each plot by a star.

Comparisons of NQR and ZFS parameters

Figure 4 shows the measured values for the ^{14}N quadrupolar splitting P and hyperfine coupling A_z plotted against the electronic ZFS parameters D and E for each NV center studied. The clear correlation illustrates the influence of local strain and electric fields on the quadrupolar Hamiltonian. The measurements cannot be explained using the Hamiltonian in eqn. (1) alone with fixed quadrupolar parameters (see Supporting Information, Sec. VII); rather, distortions of the chemical bonds cause changes in the local electric-field gradients that determine P and α . As discussed earlier, NV A exhibits ZFS parameters that are significantly shifted from the mean, consistent with a large local strain or electric field. NV A is also the only center for which we observed a nonzero α parameters in the ^{14}N quadrupolar Hamiltonian. Using Equation 4, we obtain $V_{zz} = 1.359(7) \times 10^{22} \text{ V/m}^2$, and the fitted value of α for NV A gives a normalized transverse electric field gradient value of

$$\frac{V_{XX}-V_{YY}}{V_{ZZ}} = 0.0181(3).$$

Conclusion

This study introduced a method to measure the quadrupolar Hamiltonian of an individual nucleus using a single electronic spin as a sensor. The method enabled the observation of previously unidentified terms in the ^{14}N Hamiltonian for NV centers, and elucidated correlations between the electronic and nuclear Hamiltonian parameters due to distortions of the defect's structure. Compared to existing techniques, this approach offers numerous advantages. Due to the frequency selectivity of DD spectroscopy, each nucleus is uniquely resolved by its hyperfine coupling to the electron sensor. The measurement is also highly local; its sensitivity decreases rapidly with distance since the hyperfine coupling scales as $\sim 1/d^3$, where d is the sensor-target separation; see the Supporting Information for further details on sensitivity limits. Recent advances in creating and stabilizing shallow NV centers,^{37,38} combined with this approach, can potentially allow nanoscale NQR sensors capable of probing individual nuclei at the single-molecule level. This method can also be used to probe nuclei associated with surface groups, or to fingerprint defects inside the bulk. Functionalized nanodiamonds containing NV centers can be suspended in liquid solutions and probed in biochemical environments for *in situ* and *in vivo* chemical sensing applications.³⁹⁻⁴¹

One of the significant advantages of the NV center is its surrounding ^{13}C ensemble, which can function as a quantum register^{14,42,43} and enhance sensing capacity.⁴⁴ This approach preserves the ability to utilize such techniques. Since the hyperfine and quadrupolar parameters are much stronger than the Zeeman splitting under our experimental conditions, the resonance positions remain stable over a wide range of magnetic field values. Hence, the magnetic field can be tuned for the convenience of the sample/system under study.

The accurate measurement of the asymmetry of the quadrupolar moment is becoming increasingly crucial for precise control and manipulation of quantum systems.⁴⁵⁻⁴⁷ Quadru-

lar asymmetry plays a role, for example, in semiconductor quantum dots⁴⁸ where it is the source of decoherence, and in nuclear spin squeezing⁴⁹ where it can be used for control. The ability to detect even the small magnitude of the asymmetry in systems where it is expected to be zero represents a significant advancement.

Similar to other pulsed quantum spectroscopy techniques, the sensitivity of this NQR technique is limited by T_2 and pulse errors. Pulse errors can be minimized by implementing more sophisticated control schemes.^{50,51} Although T_2 at room temperature is already close to the T_1 limit, it is possible to adapt NMR sensing protocols that surpass the T_2 limit for use with NQR.⁵² Additional techniques such as optimizing NV depth,⁵³ improving sample preparation,⁵⁴ and employing machine learning to compensate for noise⁵⁵ will further boost the sensitivity.

Methods

The sample and experimental setup are described in Refs. 56 and 57. Important details are included here.

The sample is a type-IIa electronic-grade synthetic diamond (Element Six), treated with 2-MeV electron irradiation (10^{14} cm^{-2}) and annealed at 800° C for 1 hour in forming gas. NV A is at the focus of a 6- μm -diameter solid immersion lens (SIL) surrounded by a circular antenna used for microwave control. Details on SIL fabrication are included in the Supporting Information, Sec. I.

Using the SIL around NV A, we detect ~ 0.1 photoluminescence photons per measurement shot. For other NVs that were within the antenna's range but not within the SIL's focus, we detect ~ 0.02 photons per shot, leading to reduced signal-to-noise ratio. Magnetic fields are supplied by a permanent magnet, which was aligned and calibrated using the $|m_S = 0\rangle$ to $|m_S = \pm 1\rangle$ spin-resonance transitions of NV A. For initializing the spin states, 20 μs -long green laser pulses are used to reset the system, while shorter (100 ns) laser pulses are used

to reinitialize only the electron spin.

The experiment timing was controlled by a pair of Arbitrary Waveform Generators (AWGs). One (AWG520 Tektronix) was triggered to start the experiment and controlled the optical excitations and collection paths, including the AOM used to turn on the green (532nm) laser used for readout and initialization, and the data acquisition system (National Instruments, PCIe-6323). The AWG520 was also used to trigger another AWG (AWG7102 Tektronix) which was used to control the IQ modulation of a benchtop signal generator (SG384, Stanford Research Systems), which was fed into a high bandwidth mixer (ZX05-63LH+, Mini-Circuits) to allow fast pulses and a high-isolation switch (ZASWA-2-50DR, Mini-Circuits, allowing) to prevent on-resonance leakage from decohering the spin, both of which are also controlled by the AWG7102. Interpolated pulse spacings are used to increase the resolution beyond the hardware limitations.⁵⁸ The output was fed through a USB-controlled microwave attenuator (Rudat 6000-60, Mini-Circuits) and broadband amplifier (ZHL-16W-43-S+, Mini-Circuits) before being delivered into the sample through a custom SMA-connected PCB, which is, in turn, wire-bonded to the antenna traces.

Supporting Information

Details of sample fabrication, experimental data from ESR and Ramsey experiments, dynamical decoupling spectra showing individual carbon-nuclei resonances, fitted simulations of Hamiltonian parameters, nuclear spin initialization sequences, and analysis of transverse electric field effects on the observed resonances.

Acknowledgement

This work was primarily supported by the National Science Foundation under awards ECCS-1842655 (S.A.B., T.-Y. H., and L.C.B.) and DMR-2019444 (M.O. and L.C.B.). S.A.B. acknowledges support from an IBM PhD Fellowship. M.O. acknowledges support from the

Natural Sciences and Engineering Research Council of Canada (NSERC). We thank Amelia Klein and Joseph Minnella for fruitful discussions and critical reading of our manuscript.

References

1. Das, T. P. Nuclear quadrupole resonance spectroscopy. *Solid State Physics* **1958**, *1*, 90.
2. Zax, D.; Bielecki, A.; Zilm, K.; Pines, A.; Weitekamp, D. Zero field NMR and NQR. *The Journal of chemical physics* **1985**, *83*, 4877–4905.
3. Silani, Y.; Smits, J.; Fescenko, I.; Malone, M. W.; McDowell, A. F.; Jarmola, A.; Kehayias, P.; Richards, B. A.; Mosavian, N.; Ristoff, N.; others Nuclear quadrupole resonance spectroscopy with a femtotesla diamond magnetometer. *Science Advances* **2023**, *9*, eadh3189.
4. Grechishkin, V. S.; Sinyavskii, N. Y. New technologies: nuclear quadrupole resonance as an explosive and narcotic detection technique. *Physics-Uspekhi* **1997**, *40*, 393.
5. Kim, Y.; Karaulanov, T.; Matlashov, A.; Newman, S.; Urbaitis, A.; Volegov, P.; Yoder, J.; Espy, M. Polarization enhancement technique for nuclear quadrupole resonance detection. *Solid State Nuclear Magnetic Resonance* **2014**, *61*, 35–38.
6. Malone, M. W.; Espy, M. A.; He, S.; Janicke, M. T.; Williams, R. F. The ^1H T1 dispersion curve of fentanyl citrate to identify NQR parameters. *Solid State Nuclear Magnetic Resonance* **2020**, *110*, 101697.
7. Balchin, E.; Malcolme-Lawes, D. J.; Poplett, I. J. F.; Rowe, M. D.; Smith, J. A. S.; Pearce, G. E. S.; Wren, S. A. C. Potential of Nuclear Quadrupole Resonance in Pharmaceutical Analysis. *Analytical Chemistry* **2005**, *77*, 3925–3930, PMID: 15987093.
8. Trontelj, Z.; Pirnat, J.; Jazbinšek, V.; Lužnik, J.; Srčič, S.; Lavrič, Z.; Beguš, S.; Apih, T.;

- Žagar, V.; Seliger, J. Nuclear quadrupole resonance (NQR)—a useful spectroscopic tool in pharmacy for the study of polymorphism. *Crystals* **2020**, *10*, 450.
9. Latosińska, J. N. Applications of nuclear quadrupole resonance spectroscopy in drug development. *Expert Opinion on Drug Discovery* **2007**, *2*, 225–248.
 10. Vanier, J. Nuclear quadrupole resonance thermometry. *Metrologia* **1965**, *1*, 135.
 11. Huebner, M.; Leib, J.; Eska, G. NQR on gallium single crystals for absolute thermometry at very low temperatures. *Journal of low temperature physics* **1999**, *114*, 203–230.
 12. Childress, L.; Gurudev Dutt, M.; Taylor, J.; Zibrov, A.; Jelezko, F.; Wrachtrup, J.; Hemmer, P.; Lukin, M. Coherent dynamics of coupled electron and nuclear spin qubits in diamond. *Science* **2006**, *314*, 281–285.
 13. Taminiau, T. H.; Wagenaar, J. J. T.; van der Sar, T.; Jelezko, F.; Dobrovitski, V. V.; Hanson, R. Detection and Control of Individual Nuclear Spins Using a Weakly Coupled Electron Spin. *Phys. Rev. Lett.* **2012**, *109*, 137602.
 14. Taminiau, T. H.; Cramer, J.; van der Sar, T.; Dobrovitski, V. V.; Hanson, R. Universal control and error correction in multi-qubit spin registers in diamond. *Nature Nanotechnology* **2014**, *9*, 171–176.
 15. Van der Sar, T.; Wang, Z.; Blok, M.; Bernien, H.; Taminiau, T.; Toyli, D.; Lidar, D.; Awschalom, D.; Hanson, R.; Dobrovitski, V. Decoherence-protected quantum gates for a hybrid solid-state spin register. *Nature* **2012**, *484*, 82–86.
 16. Zhao, N.; Wrachtrup, J.; Liu, R.-B. Dynamical decoupling design for identifying weakly coupled nuclear spins in a bath. *Physical Review A* **2014**, *90*, 032319.
 17. Vorobyov, V.; Javadzade, J.; Joliffe, M.; Kaiser, F.; Wrachtrup, J. Addressing single nuclear spins quantum memories by a central electron spin. *Applied Magnetic Resonance* **2022**, *53*, 1317–1330.

18. Cappellaro, P.; Jiang, L.; Hodges, J.; Lukin, M. D. Coherence and control of quantum registers based on electronic spin in a nuclear spin bath. *Physical review letters* **2009**, *102*, 210502.
19. Lang, J.; Liu, R.-B.; Monteiro, T. Dynamical-decoupling-based quantum sensing: Floquet spectroscopy. *Physical Review X* **2015**, *5*, 041016.
20. Lovchinsky, I.; Sushkov, A. O.; Urbach, E.; de Leon, N. P.; Choi, S.; Greve, K. D.; Evans, R.; Gertner, R.; Bersin, E.; Müller, C.; McGuinness, L.; Jelezko, F.; Walsworth, R. L.; Park, H.; Lukin, M. D. Nuclear magnetic resonance detection and spectroscopy of single proteins using quantum logic. *Science* **2016**, *351*, 836–841.
21. Lovchinsky, I.; Sanchez-Yamagishi, J. D.; Urbach, E. K.; Choi, S.; Fang, S.; Andersen, T. I.; Watanabe, K.; Taniguchi, T.; Bylinskii, A.; Kaxiras, E.; Kim, P.; Park, H.; Lukin, M. D. Magnetic resonance spectroscopy of an atomically thin material using a single-spin qubit. *Science* **2017**, *355*, 503–507.
22. Henshaw, J.; Kehayias, P.; Saleh Ziabari, M.; Titze, M.; Morissette, E.; Watanabe, K.; Taniguchi, T.; Li, J. I. A.; Acosta, V. M.; Bielejec, E. S.; Lilly, M. P.; Mounce, A. M. Nanoscale solid-state nuclear quadrupole resonance spectroscopy using depth-optimized nitrogen-vacancy ensembles in diamond. *Applied Physics Letters* **2022**, *120*, 174002.
23. Doherty, M. W.; Manson, N. B.; Delaney, P.; Jelezko, F.; Wrachtrup, J.; Hollenberg, L. C. The nitrogen-vacancy colour centre in diamond. *Physics Reports* **2013**, *528*, 1–45.
24. Smith, J. A. S. Nuclear quadrupole resonance spectroscopy. General principles. *Journal of Chemical Education* **1971**, *48*, 39.
25. Shin, C. S.; Butler, M. C.; Wang, H.-J.; Avalos, C. E.; Seltzer, S. J.; Liu, R.-B.; Pines, A.; Bajaj, V. S. Optically detected nuclear quadrupolar interaction of $n = 14$ in nitrogen-vacancy centers in diamond. *Physical Review B* **2014**, *89*, 205202.

26. Liu, Y.-X.; Ajoy, A.; Cappellaro, P. Nanoscale Vector dc Magnetometry via Ancilla-Assisted Frequency Up-Conversion. *Phys. Rev. Lett.* **2019**, *122*, 100501.
27. Shin, C. S.; Butler, M. C.; Wang, H.-J.; Avalos, C. E.; Seltzer, S. J.; Liu, R.-B.; Pines, A.; Bajaj, V. S. Optically detected nuclear quadrupolar interaction of ^{14}N in nitrogen-vacancy centers in diamond. *Phys. Rev. B* **2014**, *89*, 205202.
28. Bartling, H. P.; Yun, J.; Schymik, K. N.; van Riggelen, M.; Enthoven, L. A.; van Ommen, H. B.; Babaie, M.; Sebastiano, F.; Markham, M.; Twitchen, D. J.; Taminiau, T. H. Universal high-fidelity quantum gates for spin-qubits in diamond. *arXiv e-prints, quant-ph* **2024**, arxiv.org/abs/2403.10633 (accessed 2024-11-05).
29. Jamali, M.; Gerhardt, I.; Rezai, M.; Frenner, K.; Fedder, H.; Wrachtrup, J. Microscopic diamond solid-immersion-lenses fabricated around single defect centers by focused ion beam milling. *Review of Scientific Instruments* **2014**, *85*, 123703.
30. Wildanger, D.; Patton, B. R.; Schill, H.; Marseglia, L.; Hadden, J.; Knauer, S.; Schönle, A.; Rarity, J. G.; O'Brien, J. L.; Hell, S. W.; others Solid immersion facilitates fluorescence microscopy with nanometer resolution and sub-ångström emitter localization. *Advanced materials (Deerfield Beach, Fla.)* **2012**, *24*, OP309.
31. Knauer, S.; Hadden, J. P.; Rarity, J. G. In-situ measurements of fabrication induced strain in diamond photonic-structures using intrinsic colour centres. *npj Quantum Information* **2020**, *6*, 50.
32. Meesala, S.; Sohn, Y.-I.; Pingault, B.; Shao, L.; Atikian, H. A.; Holzgrafe, J.; Gündoğan, M.; Stavrakas, C.; Sipahigil, A.; Chia, C.; others Strain engineering of the silicon-vacancy center in diamond. *Physical Review B* **2018**, *97*, 205444.
33. Assumpcao, D. R.; Jin, C.; Sutula, M.; Ding, S. W.; Pham, P.; Knaut, C. M.; Bhaskar, M. K.; Panday, A.; Day, A. M.; Renaud, D.; others Deterministic creation

- of strained color centers in nanostructures via high-stress thin films. *Applied Physics Letters* **2023**, *123*, 244001.
34. Ahmed, M. A. A.; Alvarez, G. A.; Suter, D. Robustness of dynamical decoupling sequences. *Physical Review A* **2013**, *87*, 042309.
35. Busaite, L.; Lazda, R.; Berzins, A.; Auzinsh, M.; Ferber, R.; Gahbauer, F. Dynamic N 14 nuclear spin polarization in nitrogen-vacancy centers in diamond. *Physical Review B* **2020**, *102*, 224101.
36. Chakraborty, T.; Zhang, J.; Suter, D. Polarizing the electronic and nuclear spin of the NV-center in diamond in arbitrary magnetic fields: analysis of the optical pumping process. *New Journal of Physics* **2017**, *19*, 073030.
37. Neethirajan, J. N.; Hache, T.; Paone, D.; Pinto, D.; Denisenko, A.; Stoöhr, R.; Udvarhelyi, P.; Pershin, A.; Gali, A.; Wrachtrup, J.; others Controlled Surface Modification to Revive Shallow NV-Centers. *Nano Letters* **2023**, *23*, 2563–2569.
38. Kawai, S.; Yamano, H.; Sonoda, T.; Kato, K.; Buendia, J. J.; Kageura, T.; Fukuda, R.; Okada, T.; Tanii, T.; Higuchi, T.; others Nitrogen-terminated diamond surface for nanoscale NMR by shallow nitrogen-vacancy centers. *The Journal of Physical Chemistry C* **2019**, *123*, 3594–3604.
39. Shulevitz, H. J.; Amirshaghghi, A.; Ouellet, M.; Brustoloni, C.; Yang, S.; Ng, J. J.; Huang, T.-Y.; Jishkariani, D.; Murray, C. B.; Tsourkas, A.; others Nanodiamond emulsions for enhanced quantum sensing and click-chemistry conjugation. *ACS Applied Nano Materials* **2024**, *7*, 15334–15343.
40. Qin, Z.; Wang, Z.; Kong, F.; Su, J.; Huang, Z.; Zhao, P.; Chen, S.; Zhang, Q.; Shi, F.; Du, J. In situ electron paramagnetic resonance spectroscopy using single nanodiamond sensors. *Nature Communications* **2023**, *14*, 6278.

41. Holzgrafe, J.; Gu, Q.; Beitner, J.; Kara, D. M.; Knowles, H. S.; Atatüre, M. Nanoscale nmr spectroscopy using nanodiamond quantum sensors. *Physical Review Applied* **2020**, *13*, 044004.
42. Bradley, C. E.; Randall, J.; Abobeih, M. H.; Berrevoets, R. C.; Degen, M. J.; Bakker, M. A.; Markham, M.; Twitchen, D. J.; Taminiau, T. H. A Ten-Qubit Solid-State Spin Register with Quantum Memory up to One Minute. *Phys. Rev. X* **2019**, *9*, 031045.
43. Abobeih, M. H.; Randall, J.; Bradley, C. E.; Bartling, H. P.; Bakker, M. A.; Degen, M. J.; Markham, M.; Twitchen, D. J.; Taminiau, T. H. Atomic-scale imaging of a 27-nuclear-spin cluster using a quantum sensor. *Nature* **2019**, *576*, 411–415.
44. Zaiser, S.; Rendler, T.; Jakobi, I.; Wolf, T.; Lee, S.-Y.; Wagner, S.; Bergholm, V.; Schulte-Herbrüggen, T.; Neumann, P.; Wrachtrup, J. Enhancing quantum sensing sensitivity by a quantum memory. *Nature communications* **2016**, *7*, 12279.
45. Wang, J.; Paesani, S.; Santagati, R.; Knauer, S.; Gentile, A. A.; Wiebe, N.; Petruzzella, M.; O’Brien, J. L.; Rarity, J. G.; Laing, A.; others Experimental quantum Hamiltonian learning. *Nature Physics* **2017**, *13*, 551–555.
46. Gentile, A. A.; Flynn, B.; Knauer, S.; Wiebe, N.; Paesani, S.; Granade, C. E.; Rarity, J. G.; Santagati, R.; Laing, A. Learning models of quantum systems from experiments. *Nature Physics* **2021**, *17*, 837–843.
47. Nie, X.; Li, J.; Cui, J.; Luo, Z.; Huang, J.; Chen, H.; Lee, C.; Peng, X.; Du, J. Quantum simulation of interaction blockade in a two-site Bose–Hubbard system with solid quadrupolar crystal. *New Journal of Physics* **2015**, *17*, 053028.
48. Hackmann, J.; Glasenapp, P.; Greilich, A.; Bayer, M.; Anders, F. Influence of the nuclear electric quadrupolar interaction on the coherence time of hole and electron spins confined in semiconductor quantum dots. *Physical Review Letters* **2015**, *115*, 207401.

49. Korkmaz, Y. A.; Bulutay, C. Nuclear spin squeezing via electric quadrupole interaction. *Physical Review A* **2016**, *93*, 013812.
50. Arroyo-Camejo, S.; Lazariev, A.; Hell, S. W.; Balasubramanian, G. Room temperature high-fidelity holonomic single-qubit gate on a solid-state spin. *Nature communications* **2014**, *5*, 4870.
51. Rong, X.; Geng, J.; Shi, F.; Liu, Y.; Xu, K.; Ma, W.; Kong, F.; Jiang, Z.; Wu, Y.; Du, J. Experimental fault-tolerant universal quantum gates with solid-state spins under ambient conditions. *Nature communications* **2015**, *6*, 8748.
52. Schwartz, I.; Roskopf, J.; Schmitt, S.; Tratzmiller, B.; Chen, Q.; McGuinness, L. P.; Jelezko, F.; Plenio, M. B. Blueprint for nanoscale NMR. *Scientific Reports* **2019**, *9*, 6938.
53. DeVience, S. J.; Pham, L. M.; Lovchinsky, I.; Sushkov, A. O.; Bar-Gill, N.; Belthangady, C.; Casola, F.; Corbett, M.; Zhang, H.; Lukin, M.; others Nanoscale NMR spectroscopy and imaging of multiple nuclear species. *Nature nanotechnology* **2015**, *10*, 129–134.
54. Cohen, D.; Nigmatullin, R.; Eldar, M.; Retzker, A. Confined Nano-NMR Spectroscopy Using NV Centers. *Advanced Quantum Technologies* **2020**, *3*, 2000019.
55. Aharon, N.; Rotem, A.; McGuinness, L. P.; Jelezko, F.; Retzker, A.; Ringel, Z. NV center based nano-NMR enhanced by deep learning. *Scientific reports* **2019**, *9*, 17802.
56. Hopper, D. A.; Grote, R. R.; Exarhos, A. L.; Bassett, L. C. Near-infrared-assisted charge control and spin readout of the nitrogen-vacancy center in diamond. *Physical Review B* **2016**, *94*, 241201.
57. Hopper, D. A.; Lauigan, J. D.; Huang, T.-Y.; Bassett, L. C. Real-Time Charge Initial-

ization of Diamond Nitrogen-Vacancy Centers for Enhanced Spin Readout. *Phys. Rev. Appl.* **2020**, *13*, 024016.

58. Ajoy, A.; Liu, Y.-X.; Saha, K.; Marseglia, L.; Jaskula, J.-C.; Bissbort, U.; Cappellaro, P. Quantum interpolation for high-resolution sensing. *Proceedings of the National Academy of Sciences* **2017**, *114*, 2149–2153.

Supporting Information: Quadrupolar resonance spectroscopy of individual nuclei using a room-temperature quantum sensor

S. Alex Breitweiser,^{1,2,*} Mathieu Ouellet,^{1,*} Tzu-Yung Huang,^{1,†} Tim H. Taminiau,^{3,4} and Lee C. Bassett^{1,‡}

¹*Quantum Engineering Laboratory, Department of Electrical and Systems Engineering,
University of Pennsylvania, 200 S. 33rd St. Philadelphia, Pennsylvania, 19104, USA* §

²*Department of Physics and Astronomy, University of Pennsylvania,
209 S. 33rd St. Philadelphia, Pennsylvania 19104, USA*

³*QuTech, Delft University of Technology, PO Box 5046, 2600, GA Delft, The Netherlands*

⁴*Kavli Institute of Nanoscience Delft, Delft University of Technology,
PO Box 5046, 2600, GA Delft, The Netherlands*

(Dated: January 11, 2025)

I. SAMPLE FABRICATION

The sample and setup are the same as those described in Refs. 1 and 2. In order to increase the photon collection efficiency, NV-A is located at the center of a 6- μm -diameter solid immersion lens (SIL). To align and fabricate the SIL, we first spin-coated a 500 nm layer of PMMA A8 resist (MicroChem Nano PMMA) onto the diamond surface without baking the resist. After identifying a candidate NV in our confocal microscope, we used the 532 nm excitation laser to burn five holes into the PMMA: four marking the corners of an 8- μm bounding box, and one centered over the NV center. Next, we sputtered a layer of AuPd onto the PMMA to mitigate charging during SIL fabrication. The sample was then loaded into a dual-beam scanning electron microscope and focused ion beam system (SEM/FIB, Strata D235, FEI), where the alignment marks were identified and the SIL was milled. After milling, a gallium-implanted layer remains on the diamond surface, which we removed by etching 80 nm of diamond using an Ar/Cl ICP/RIE process (Trion Phantom ICP, Pressure: 10 mT, ICP: 400 W, RIE: 300 W, Ar: 12 sccm, Cl₂: 20 sccm) [3]. Finally, the sample was cleaned in Nanostrip (Cyantek) at 70° C for 20 minutes, followed by a soft O₂ plasma clean for 15 minutes (Anatech SCE-108 Barrel Asher, RF power = 30 W) to remove any graphite and to oxygen-terminate the surface. The microwave antenna was subsequently fabricated using standard optical lithography.

II. ESR AND RAMSEY EXPERIMENTS

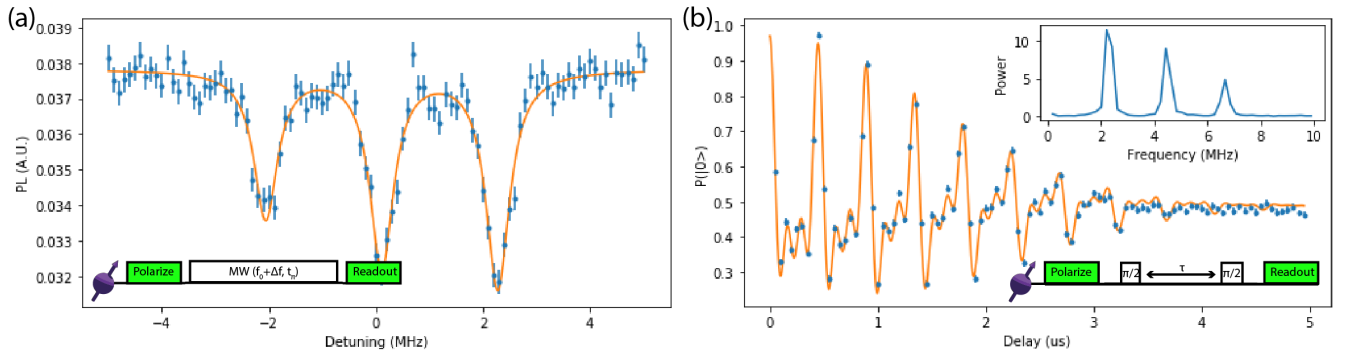


FIG. S1. (a) Pulsed ESR and (b) Ramsey data (blue points) from NV A taken with an on-axis field ($B_Z > 0$). Fits (solid orange lines) are consistent with a model containing only the nitrogen-14 nuclear spin coupling, with no other strongly coupled spins detected.

* These two authors contributed equally

† Present address: Nokia Bell Labs, 600 Mountain Avenue, Murray Hill, NJ 07974, USA

‡ lbassett@seas.upenn.edu

§ Present address: IBM Research, 1101 Kitchawan Rd Yorktown Heights, NY 10598, USA

With natural isotopic abundance, we expect around 1.1% of the carbon nuclei in the diamond lattice to be carbon-13. In bulk electronics grade samples, this means we expect a "typical" NV center to have a few carbon-13 nuclei coupled in the $2\pi \times 10 - 100$ kHz range, as well as the NV's intrinsic nitrogen-14 nucleus with $\approx 2\pi \times 2.17$ MHz coupling. It is possible to have more strongly coupled carbon-13 nuclei if one is located within the first few coordination shells around the NV center, which causes both the dipolar and contact couplings to increase. Two simple methods for measuring strong nuclear couplings are electron spin resonance (ESR) and Ramsey type experiments. These related experiments use either a weak, detuned microwave pulse or measure the rotation of a coherent electron superposition state to infer the energy levels of the electron spin. Since these are shifted by the coupling to nuclear spin, different frequencies will be observed. Both of these are limited in resolution by the coherence time of the electron, either under driving (T_2^{Rabi}) or free decay (T_2^*), which are expected to be similar.

Fig. S1 shows ESR and Ramsey data on NV A with an on axis magnetic field. In Fig. S1(a), ESR is taken with $1 \mu\text{s}$ pulse widths at an amplitude which gives an approximate π rotation, leading to an ≈ 1 MHz resolution. While this does not saturate the coherence limit, this avoids broadening of the peaks due to slow spectral drift in the system. In Fig. S1, the phase of the final $\frac{\pi}{2}$ pulse is swept at 5 MHz to aid in measuring the component oscillation frequencies of the beating signal. Data was taken past $T_2^* \approx 2.4(1) \mu\text{s}$ and showed no revivals. Both of these datasets are consistent with a model including only the nitrogen-14 nuclear spin and no other strongly coupled nuclei ($|A_Z| \gtrsim \frac{2\pi}{T_2^*} \approx 2\pi \times 300$ kHz, where $|A_Z|$ is the strength of the on-axis component of the electro-nuclear hyperfine coupling). Datasets for the other NVs studied were similar, either showing no strong couplings or only a few couplings near the T_2^* limit for those with longer coherence times. None showed Carbon-13 couplings stronger than 200 kHz.

III. DYNAMICAL DECOUPLING SPECTRUM

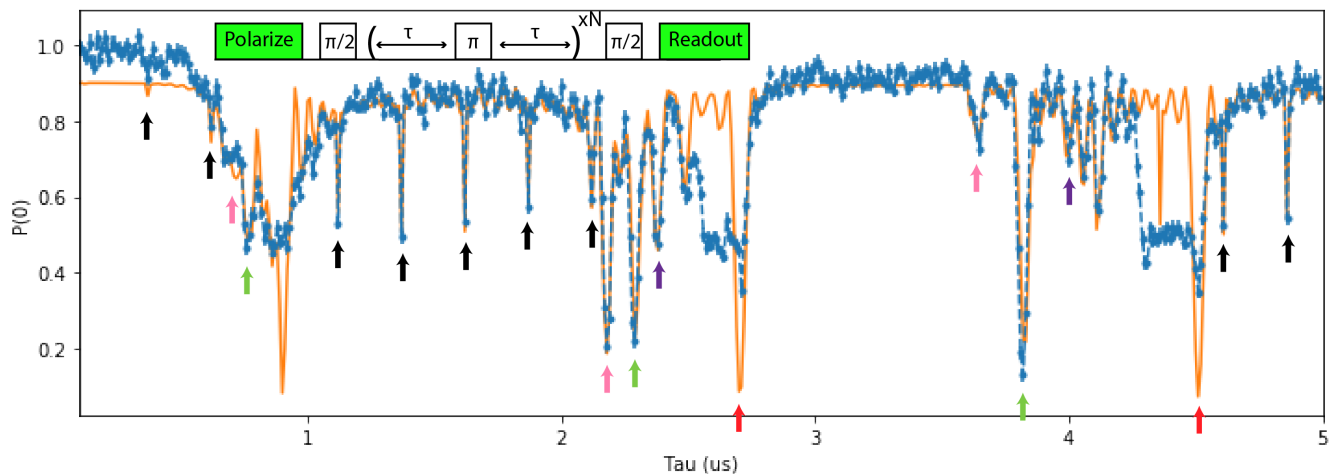


FIG. S2. Dynamical decoupling data (blue points w/ dashed line) taken on NV A with a purely on-axis field ($B_X \approx 0$) shows resonances associated with multiple individual carbon-nuclei (colored arrows), as well as a resonance series associated with a higher energy spin (black arrows). Simulation (solid yellow line) shows this is consistent with an additional term in the nitrogen-14 nuclear quadrupolar Hamiltonian, as well as the known carbon-13 nuclei. Data is taken with $N = 32$ pulses at a magnetic field of 264 Gauss aligned within $\approx 1^\circ$ of the NV axis. (Inset) High-resolution data (markers) taken for various N around $\tau = 1.372 \mu\text{s}$ fitted using our in-house simulator (best-fit simulation represented by dashed lines). Based on this we determine $\alpha = 2\pi \times 2.43(2)$ kHz for the Nitrogen-14 nuclear spin.

Dynamical decoupling extends the coherence time of the electron spin with refocusing pulses. A single refocusing pulse is enough to extend the coherence time to several hundred μs , greatly increasing the resolution with which nuclear spin dynamics can be detected in spectroscopy. Furthermore, at higher pulse numbers and longer inter-pulse spacings, resonances from individual nuclei become sharper and separate spectrally, allowing resonances from weakly coupled nuclei to be observed. In the case of spin- $\frac{1}{2}$ nuclei such as ^{13}C , the approximate location of individual nuclear spin resonances is given by

$$\tau_k = \frac{(2k-1)\pi}{2\omega_L + A_Z} \quad (1)$$

where τ_k is the spacing between pulses at the k -th resonance, ω_L is the nuclear Larmor frequency, and A_Z is the parallel component of the hyperfine coupling for that individual nuclei. Spectroscopy from sweeping τ is then expected to reveal resonances arising from several more weakly coupled C-13 nuclei (with $\frac{2\pi}{T_2} \gtrsim |A_Z| \gtrsim \frac{2\pi}{T_2} \approx 2\pi \times 10$ kHz) for an NV in natural isotopic abundance diamond, such as those in the sample under study.

Indeed, we observe resonances associated with at least four C-13 nuclei within the dynamical decoupling spectroscopy data shown in Fig. S2, indicated by colored arrows. Additional data was taken at each resonance and fitted in simulation to obtain the hyperfine coupling for each carbon-13. In addition, broad resonances saturating to $P(|0\rangle) = 0.5$ are caused by the electron spin entangling with a large number of nuclei near the carbon-13 Larmor frequency. Here, data is taken with a purely on-axis magnetic field ($B_X \approx 0$), and therefore, resonances associated with the $m_I = 0$ to $m_I = \pm 1$ nitrogen nuclear spin transition are not expected to appear. However, the data also contain an unexpected, higher-frequency resonance series in addition to the expected carbon-13 resonances. The resonance series corresponds to a frequency of several MHz, and it is stable to the reorientation of the external DC magnetic field (up to at least $\pm 3^\circ$). Additional data was taken around one of these resonances and fitted to obtain the α and A parameters for the nitrogen-14 nuclear spin Hamiltonian in NV A as described in Fig. 2 of the main text. After fitting the four carbon-13 nuclear resonances and the nitrogen-14 nuclear parameters (including the P and A parameters) the simulations (yellow line) agree well with the dynamical decoupling spectra everywhere except near the carbon-13 Larmor frequency (which is expected as our exact simulations do not account for the nuclear spin bath).

Other NVs studied in this work showed similar carbon-13 resonances but did not display the high-frequency resonances associated with the nitrogen nuclear spin.

IV. FITTING ADDITIONAL HAMILTONIAN PARAMETERS FOR NITROGEN-14 NUCLEI

As described in the main text, data was taken for each NV with a slightly off-axis field ($|B_X| > 0$), allowing $m_I = 0$ to $m_I = \pm 1$ nitrogen nuclear spin transitions to occur due to spin mixing. To fit the value of both the hyperfine and quadrupolar parameters of the Nitrogen nuclear spins in the NVs studied, the number of Dynamical Decoupling pulses was swept while looking at a narrow region around a high order resonances for each of the two transitions. The resonances were chosen to avoid features related to Carbon-13 nuclei coupled to each NV. The data for both resonances was simultaneously fitted to a simulation based on the Hamiltonian given in the main text for each NV, with the hyperfine and quadrupolar parameters allowed to vary. Additional variation parameters were added to account for the loss of coherence due to pulse imperfections and dephasing of the NV electron spin during the DD sequence. Data for each NV listed in the main text is shown in figure Fig. S3.

V. NUCLEAR SPIN INITIALIZATION AND TOMOGRAPHY SEQUENCES

Based on our fitted simulations, we find that $N = 24$ pulses at a spacing of $\tau = 1.372$ us gives an approximate $\frac{\pi}{2}$ rotation between the $|m_I = -1\rangle$ and $|m_I = +1\rangle$ states of the Nitrogen-14 nuclear spin conditional on the state of the electron spin within the $|m_S = 0\rangle / |m_S = -1\rangle$ manifold (see Fig1(b) of main text). Furthermore, simulations show that a high-fidelity unconditional Z rotation on the $|m_I = \pm 1\rangle$ manifold of the Nitrogen-14 spin can be implemented using a single pulse on the $|m_S = 0\rangle / |m_S = -1\rangle$ electron spin manifold, due to the small magnitude of the off-axis term in the nuclear quadrupolar Hamiltonian.

Using these two-qubit gates, we implement nuclear initialization and tomography sequences adapted from [5], as depicted in Fig. S4.

VI. INITIALIZED RAMSEY

As described in the main text, Ramsey data was taken after initializing the nitrogen nuclear spin using the above sequence to measure the population in each nuclear spin states. To ensure we are not observing a steady state polarization, the amount of green time used to re-initialize the electron spin is swept. Raw Ramsey data for each electron re-initialization length is shown in Fig. S5. Data for the steady state Ramsey is repeated from Fig. S1 As expected, the nuclear spin populations decay back to the steady state value due to off-axis hyperfine coupling in the excited electronic state, with a characteristic decay time of several μs (similar to other published work [6]).

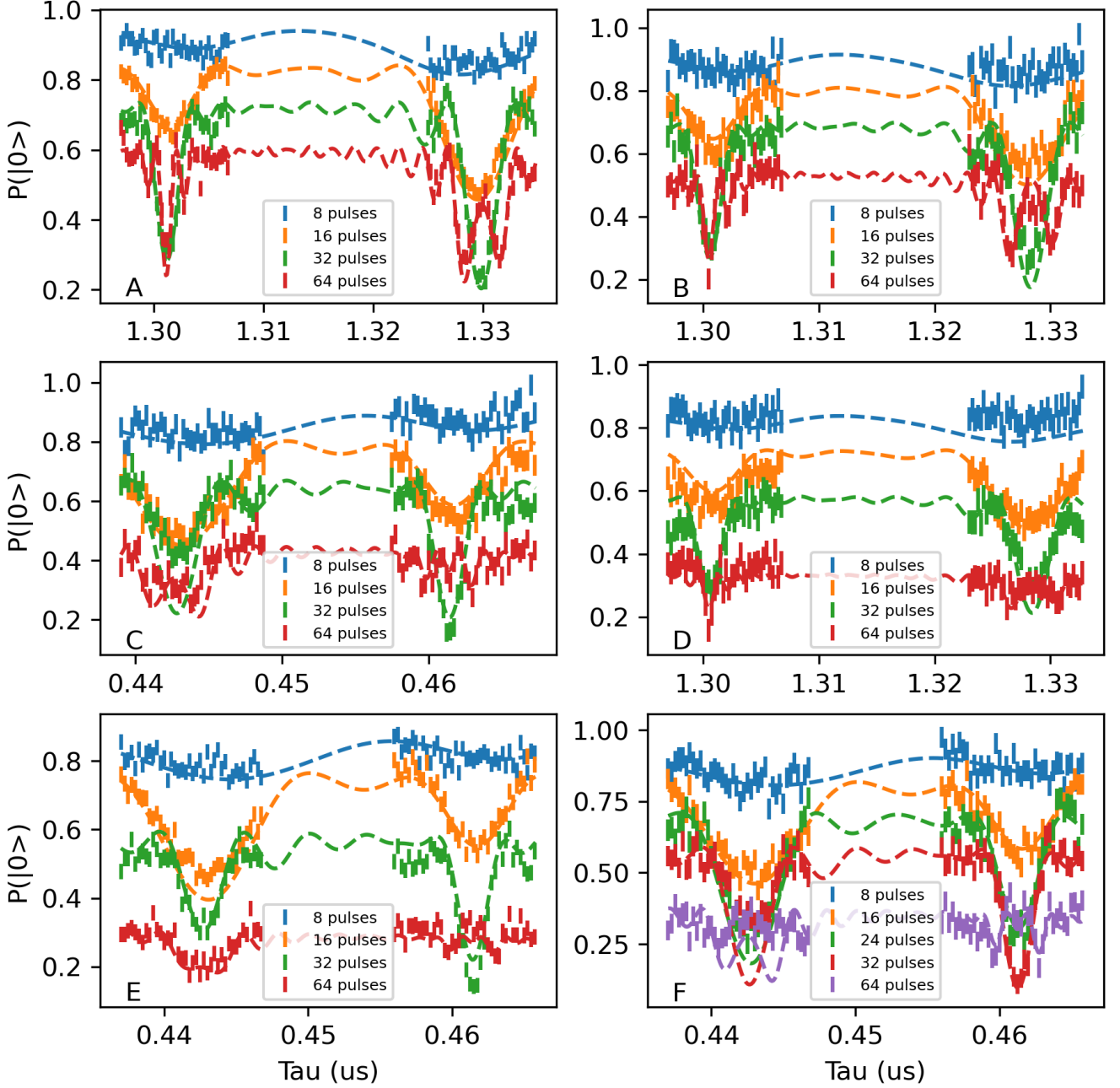


FIG. S3. Dynamical decoupling data for each NV studied taken with an off-axis field $|B_X| > 0$, showing resonances associated with $|m_I = 0\rangle$ to $|m_I = \pm 1\rangle$ transitions of the Nitrogen-14 nuclear spin as the number of dynamical decoupling pulses is swept. Pulse spacings below the hardware limit (≈ 1 ns) are achieved using interpolated sequences [4]

VII. FULL NITROGEN INITIALIZATION

A. Simulations

Simulations throughout the manuscript were performed using exact simulation of the described Hamiltonians, along with the well-known Hamiltonian for the electronic spin of the negatively charged NV center at room temperature. Only spin degrees of freedom are considered, while optical and charge dynamics are assumed to be normalized away by readout calibrations which are interleaved with the experiments. Decoherence dynamics are modeled as a uniform decay of this signal, using the form described in Equation (8) of the main text. Hyperfine and quadrupolar parameters

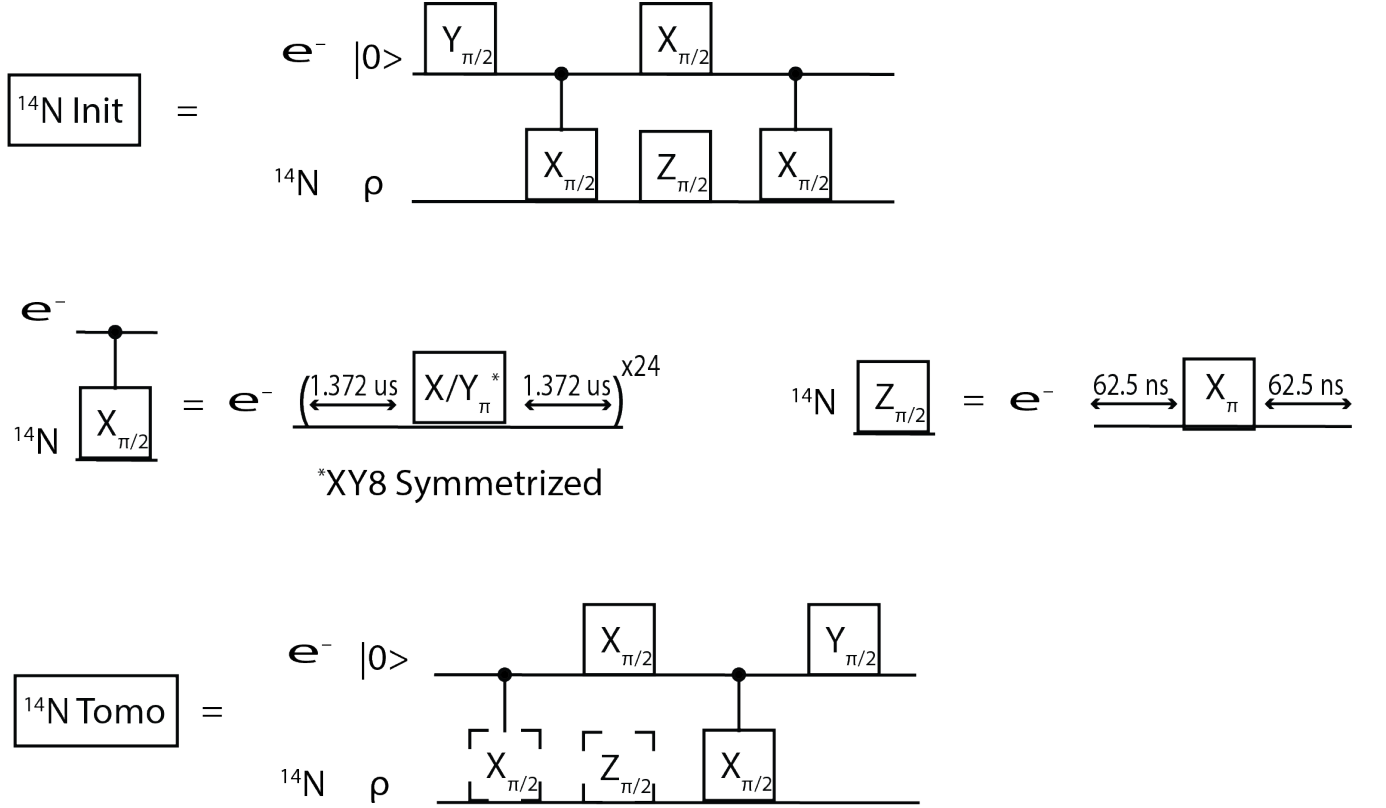


FIG. S4. Sequences used to initialize and read out the nuclear spin state using the electron spin. Dashed gates in the tomography sequence are included or removed depending on the desired nuclear measurement axis.

are extracted from data by allowing these parameters to vary in the simulations and fitting the simulation results to the data using general optimization methods.

In Figure 4, simulations are performed without (a) and with (b) Gaussian noise, which is representative of the dominant shot noise in our experiments. In Figure 4(a), the maximum contrast is obtained by sweeping the number of pulses and measuring the largest contrast obtained, where contrast is defined as the depth of the resonance peak divided by the total readout contrast (normalized to be 1). In Figure 4(b), simulations were performed and random noise was added in, using a noise amount characteristic of our experiments. For each value of β , the α parameter in simulation was reduced until the uncertainty in the fit dropped below the actual signal.

B. Resonant Lines for α

The Hamiltonian of the system is given by:

$$\begin{aligned}
 H &= H_{ZE} + H_{ZN} + H_{hf} + H_{\text{quad}} \\
 H_{\text{quad}} &:= P(I_Z^2) + \alpha(I_+^2 + I_-^2) \\
 H_{hf} &:= A_Z S_Z I_Z + A_{\perp} S_Z I_X \\
 H_{ZE} &:= \Omega_E S_Z \\
 H_{ZN} &:= \Omega_N I_Z
 \end{aligned}$$

where H_{ZE} and H_{ZN} represent the Zeeman terms for the electronic and nitrogen spins, respectively, H_{quad} denotes the quadrupolar term, and H_{hf} refers to the hyperfine coupling between the two spins.

Under the assumption that the perpendicular hyperfine coupling is negligible, i.e., $A_{\perp} \approx 0$, we can perform a unitary transformation $U(t)$ to eliminate all the fast-rotating components from the system. The transformation is given by $U(t) = e^{-i\Delta_E t S_z} \otimes e^{-i\Delta_N t I_z}$. The transformation is described by $U(t) = e^{-i\Delta_E t S_z} \otimes e^{-i\Delta_N t I_z}$. Under this transformation, the terms H_{ZE} , H_{ZN} , and $H_{hf,Z}$ remain unchanged. Contrary to the isotropic components of the

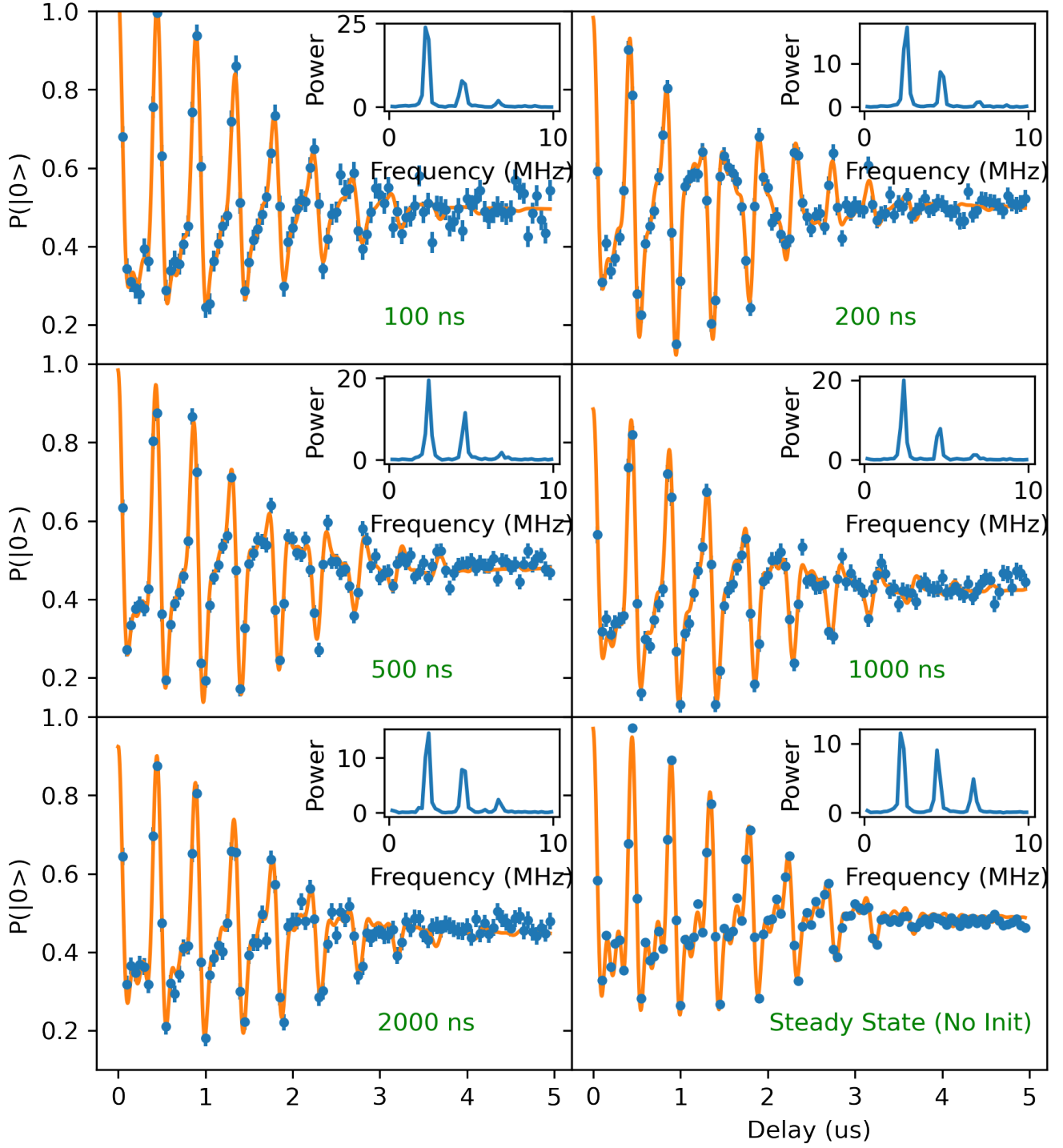


FIG. S5. Initialized Ramsey experiment for each of the electron re-initialization times, as depicted in Fig3(a) of the main text. Blue markers are data and yellow lines are oscillatory fits used to extract the occupation parameters of the Nitrogen-14 spin. (Insets) Power spectra for each of the Ramsey experiments - the polarization of the Nitrogen-14 spin is apparent from the unequal height of the frequency peaks.

Hamiltonian, the quadrupolar coupling does not commute with the other terms. As a result, it is essential to calculate its contribution to the Hamiltonian explicitly. Using the Baker–Campbell–Hausdorff formula, we get that

$$\begin{aligned} e^{i\lambda I_z} I_+^2 e^{-i\lambda I_z} &= e^{2i\lambda} I_+^2 \\ e^{i\lambda I_z} I_-^2 e^{-i\lambda I_z} &= e^{-2i\lambda} I_-^2 \end{aligned}$$

Thus, the Hamiltonian expressed in the rotating frame is given by:

$$H' = A_Z S_Z I_Z + P(I_Z^2) + \alpha(e^{2i\Delta_N} I_+^2 + e^{-2i\Delta_N} I_-^2)$$

where we set $\Delta_E = \Omega_E$ and $\Delta_N = \Omega_N$. The term that is dependent on the electronic spin state is solely given by $A_Z S_Z I_Z = A_Z [|1\rangle\langle 1| - |-1\rangle\langle -1|] \otimes I_Z$ which allows us to write the Hamiltonian as

$$H' = |-1\rangle\langle -1| \otimes H_{-1} + |0\rangle\langle 0| \otimes H_0 + |1\rangle\langle 1| \otimes H_1$$

where $H_{-1} = -A_Z I_z + H_{ind}$, $H_0 = H_{ind}$, and $H_1 = A_Z I_z + H_{ind}$. We have consolidated the time-independent portion of the Hamiltonian into H_{ind} , which includes the quadrupolar term and is expressed as:

$$H_{ind} = P(I_Z^2) + \alpha(e^{2i\Delta_N} I_+^2 + e^{-2i\Delta_N} I_-^2)$$

The evolution operator $V = \exp\{-iHt\}$ takes the same form

$$V = |-1\rangle\langle -1| \otimes V_{-1} + |0\rangle\langle 0| \otimes V_0 + |1\rangle\langle 1| \otimes V_1,$$

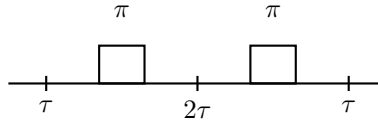
where V_i exclusively influences the nitrogen subspace with spin state i and can be formulated as a rotation around an axis \vec{n}_i of angle ϕ_i such that $V_i = \exp[-i\phi_i(\vec{I} \cdot \vec{n}_i)]$. For a spin 1 system, the trace is computed as

$$\text{Tr} \left[\exp \left[-i\phi_i(\vec{I} \cdot \vec{n}) \right] \right] = 1 + 2 \cos \phi_i.$$

Our goal is to isolate $\vec{n}_i \cdot \vec{n}_j$ to allow us to find the resonance conditions. To do so, we can use the fact that $\text{Tr} \left[\exp \left[-i\phi(\vec{I} \cdot \vec{n}) \right] I_j \right] = -2i \sin(\phi) n_j$ to generate this expression

$$\vec{n}_{-1} \cdot \vec{n}_0 = 1 + \frac{1}{4} \sum_{j \in \{x, y, z\}} \frac{\text{Tr}[(V_{-1} - V_0)I_j] \text{Tr}[(V_{-1}I_j)]}{1 - \left(\frac{\text{Tr}[V_0]-1}{2}\right)^2}$$

Under a π -pulse, using the $|-1\rangle, |0\rangle$ as an example the electronic spin evolves as follows: $|-1\rangle \rightarrow |0\rangle$, $|+1\rangle \rightarrow |+1\rangle$, and $|0\rangle \rightarrow |-1\rangle$, with the pulse sequence specified by:



This results in the following evolution operators:

$$\begin{aligned} V_0 &= \exp[-i\tau H_{ind}] \exp[-2i\tau H_{+1}] \exp[-i\tau H_{ind}] \\ V_{-1} &= \exp[-4i\tau H_{-1}] \\ V_{+1} &= \exp[-i\tau H_{+1}] \exp[-2i\tau H_{ind}] \exp[-i\tau H_{+1}]. \end{aligned}$$

Our objective is to determine the difference in rotation between the $+1$ and -1 states, which can be computed as $\vec{n}_{-1} \cdot \vec{n}_{+1}$ and the angle of rotation ϕ . It is important to note that our aim is not to maximize the angle ϕ but rather to find the condition that maximizes the difference in the evolution of the states $|+1\rangle\langle +1|$ and $|-1\rangle\langle -1|$. Our goal is, therefore, to minimize the dot product between those two angles:

$$\tau_{res} = \arg \min_{\tau} \left(1 + \frac{1}{4} \sum_{j \in \{x, y, z\}} \frac{\text{Tr}[(V_{+1} - V_{-1})I_j] \text{Tr}[(V_{+1}I_j)]}{1 - \left(\frac{\text{Tr}[V_{-1}]-1}{2}\right)^2} \right)$$

Minimizing this equation is laborious, yet several small parameters are present in the Hamiltonian. The hyperfine coupling significantly outweighs the Zeeman term ($\frac{\Omega_N}{A_Z} \approx 0.04$), allowing for a first-order expansion of the ratio. Similarly, for $\frac{\alpha}{\Omega_N} \approx 0.03$, retaining the term at first order is appropriate, while the term $\frac{\alpha}{A_Z}$ can be safely omitted, as it is approximately 0.001.

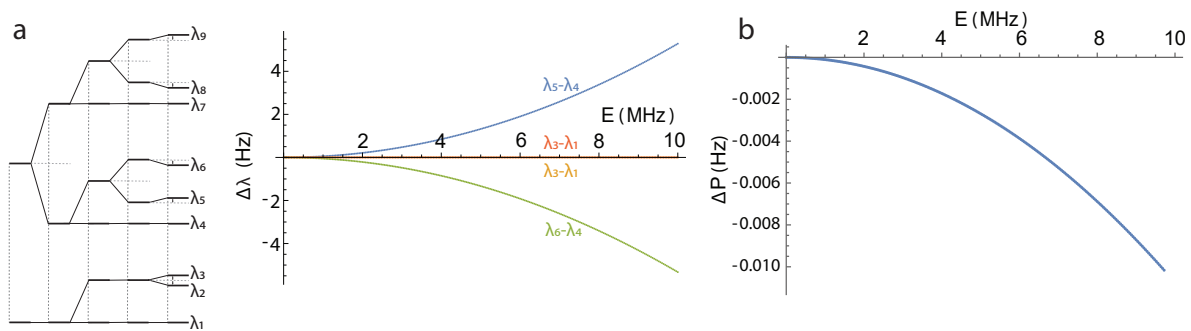


FIG. S6. Effect of a transverse electric or strain field (a) on the relative energy spacings in the $m_s = 0$ and $m_s = -1$ subspaces and (b) on the inferred nuclear quadrupolar splitting, P , as a function of the transverse zero-field splitting parameter, E .

VIII. TRANSVERSE ELECTRIC OR STRAIN FIELDS

In this section, we consider potential contributions to the full electron-nuclear Hamiltonian and corresponding dynamics due to transverse electric fields or transverse strain fields. Transverse strain or electric fields break the NV center's symmetry [7], distorting the electron cloud and perturbing the zero-field electron-Hamiltonian parameters D and E (of which the latter should be strictly zero in the absence of such perturbation). In principle, these perturbations can combine with the hyperfine coupling to create second-order perturbations of the coupled electron-nuclear eigenstates and their corresponding energies. It is therefore important to confirm that the variations we observe in experiments cannot be explained by such perturbations.

Figure S6(a) shows the variation of the relative energy splittings within the $m_s = 0$ and $m_s = -1$ manifolds as a function of the electronic transverse perturbation, E_x . We observe that the transverse electronic term does indeed mix and perturb the coupled electron-nuclear states. However, for values of E on the scale of ~ 10 MHz, as measured in our experiments, the corresponding perturbations are on the scale of a few hertz, which is several orders of magnitude smaller than the kHz-scale variations we observe in measurements of P and A_z (see Fig. 4 in the main text). Moreover, the perturbation tends to couple predominantly the $m_I = 0$ states with $m_I = \pm 1$, such that the energy differences associated with $\Delta m_I = \pm 1$ transitions evolve in opposite directions. In contrast, the longitudinal quadrupolar term P shifts both transitions in the same direction. Figure S6(b) illustrates this effect, where the change in effective P caused by transverse strain perturbations (effectively, the common-mode variation of the $m_I = \pm 1$ levels compared to $m_I = 0$) remains well below 1 Hz for relevant perturbation strengths. Higher-order electric-field perturbations (e.g., with an electronic Hamiltonian term proportional to $S_Z S_X$) are typically neglected [8], and they result in an even smaller shift in the measured quadrupolar splitting.

Since the transverse-strain perturbations appear in the full Hamiltonian (Eq. 1 in the main text) as terms that couple $m_I = 0$ states with $m_I = \pm 1$ states, they are physically distinct from the nuclear quadrupolar asymmetry term, α , which directly couples $m_I = \pm 1$. In this way, their effect would be similar (albeit smaller in magnitude) to the effect of an off-axis magnetic field, which also indirectly couples the states with $\Delta m_I = 1$. We have verified through simulations that such terms in the Hamiltonian cannot account for the regular series of dips that are associated with the direct $\Delta m_I = 2$ transitions between states with $m_I = \pm 1$. This analysis further supports the interpretation of our model in capturing the observed frequency shifts in terms of variations in the nuclear quadrupolar Hamiltonian.

-
- [1] David A Hopper, Richard R Grote, Annemarie L Exarhos, and Lee C Bassett. Near-infrared-assisted charge control and spin readout of the nitrogen-vacancy center in diamond. *Physical Review B*, 94(24):241201, 2016.
 - [2] David A. Hopper, Joseph D. Lauigan, Tzu-Yung Huang, and Lee C. Bassett. Real-time charge initialization of diamond nitrogen-vacancy centers for enhanced spin readout. *Phys. Rev. Appl.*, 13:024016, Feb 2020.
 - [3] Mohammad Jamali, Ilja Gerhardt, Mohammad Rezai, Karsten Frenner, Helmut Fedder, and Jörg Wrachtrup. Microscopic diamond solid-immersion-lenses fabricated around single defect centers by focused ion beam milling. *Review of Scientific Instruments*, 85(12), 2014.
 - [4] Ashok Ajoy, Yi-Xiang Liu, Kasturi Saha, Luca Marseglia, Jean-Christophe Jaskula, Ulf Bissbort, and Paola Cappellaro. Quantum interpolation for high-resolution sensing. *Proceedings of the National Academy of Sciences*, 114(9):2149–2153, 2017.
 - [5] T. H. Taminiau, J. Cramer, T. van der Sar, V. V. Dobrovitski, and R. Hanson. Universal control and error correction in

- multi-qubit spin registers in diamond. *Nature Nanotechnology*, 9(3):171–176, Mar 2014.
- [6] Tanmoy Chakraborty, Jingfu Zhang, and Dieter Suter. Polarizing the electronic and nuclear spin of the NV-center in diamond in arbitrary magnetic fields: analysis of the optical pumping process. *New Journal of Physics*, 19(7):073030, jul 2017.
- [7] Florian Dolde, Helmut Fedder, Marcus W Doherty, Tobias Nöbauer, Florian Rempp, Gopalakrishnan Balasubramanian, Thomas Wolf, Friedemann Reinhard, Lloyd CL Hollenberg, Fedor Jelezko, et al. Electric-field sensing using single diamond spins. *Nature Physics*, 7(6):459–463, 2011.
- [8] Eric Van Oort and Max Glasbeek. Electric-field-induced modulation of spin echoes of nv centers in diamond. *Chemical Physics Letters*, 168(6):529–532, 1990.

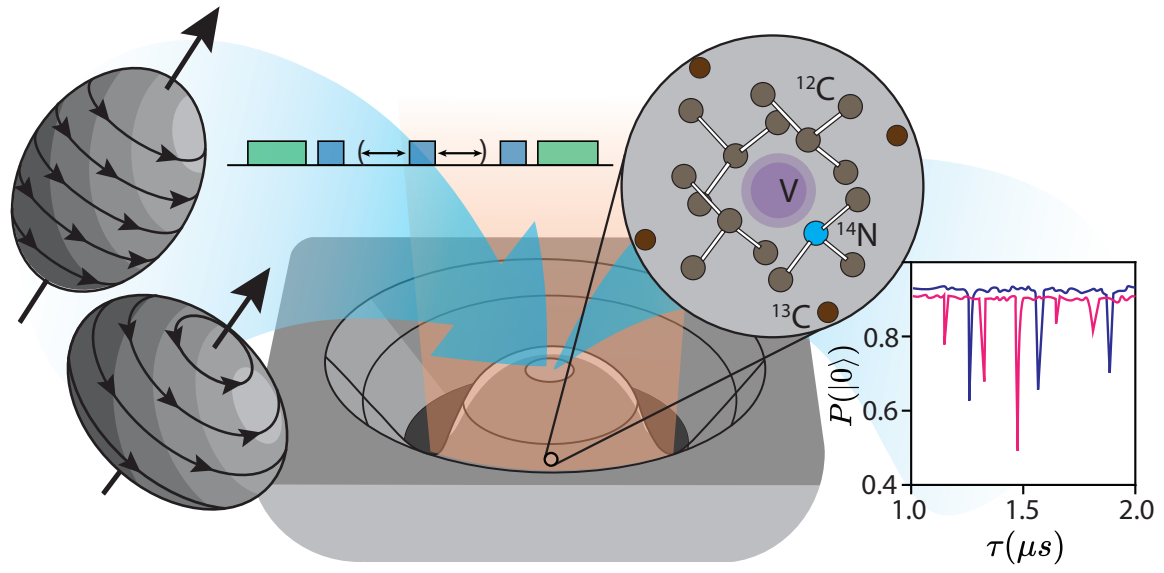


Figure 5: TOC Graphic